crystals

MDPI

Article

Enhancing Salt Stress Tolerance in Rye with ZnO Nanoparticles: Detecting H_2O_2 as a Stress Biomarker by Nanostructured NiO Electrochemical Sensor

Vjaceslavs Gerbreders, Marina Krasovska *, Eriks Sledevskis, Irena Mihailova, Valdis Mizers, Jans Keviss and Andrejs Bulanovs

G. Liberts' Innovative Microscopy Centre, Department of Technology, Institute of Life Sciences and Technology, Daugavpils University, 1a Parades Str., LV-5401 Daugavpils, Latvia; vjaceslavs.gerbreders@du.lv (V.G.); eriks.sledevskis@du.lv (E.S.); irena.mihailova@du.lv (I.M.); valdis.mizers@du.lv (V.M.); jans.keviss@du.lv (J.K.); andrejs.bulanovs@du.lv (A.B.)

* Correspondence: marina.krasovska@du.lv

Abstract: This article is devoted to the study of the effect of ZnO nanoparticles on the development of tolerance to salt stress in rye samples. As a quantitative criterion for assessing the degree of oxidative stress, the amount of H_2O_2 released in the samples during growth was determined. For these purposes, an electrochemical sensor based on hydrothermally synthesized wall-shaped NiO nanostructures was developed. This sensor has been proven to demonstrate high sensitivity (2474 $\mu A \cdot mM^{-1}$), a low limit of detection (1.59 μM), good selectivity against common interferents, and excellent long-term stability. The investigation reveals that the incorporation of ZnO nanoparticles in irrigation water notably enhances rye's ability to combat salt stress, resulting in a decrease in detected H_2O_2 levels (up to 70%), coupled with beneficial effects on morphological traits and photosynthetic rates.

Keywords: ZnO nanoparticles; NiO wall-shaped nanostructures; hydrothermal synthesis; electrochemical sensor; H_2O_2 detection; salt stress; oxidative stress; stress tolerance; rye

Citation: Gerbreders, V.; Krasovska, M.; Sledevskis, E.; Mihailova, I.; Mizers, V.; Keviss, J.; Bulanovs, A. Enhancing Salt Stress Tolerance in Rye with ZnO Nanoparticles: Detecting H_2O_2 as a Stress Biomarker by Nanostructured NiO Electrochemical Sensor. *Crystals* **2024**, *14*, 423. https://doi.org/10.3390/cryst14050423

Academic Editor: Yusuf Valentino Kaneti

Received: 12 April 2024
Revised: 25 April 2024
Accepted: 28 April 2024
Published: 29 April 2024

1. Introduction

Abiotic stress factors, encompassing drought [1,2], salinity [3,4], extreme temperatures [5], and heavy metals [6], profoundly impact plant growth and development, disrupting cellular homeostasis and inducing oxidative stress [7–9]. Among the various reactive oxygen species (ROS) generated, hydrogen peroxide (H_2O_2) stands out as a critical signaling molecule [10] and stress biomarker in plants exposed to such adversities [11–13]. Elevated levels of H_2O_2 within plant cells signify an imbalance between ROS production and scavenging mechanisms, triggering an intricate cascade of responses to counteract stress effects [14]. Stress tolerance development in plants involves a multifaceted array of adaptive strategies [15–17]. Morphological adaptations [18,19], such as alterations in root architecture and leaf structure, aid in water acquisition and conservation. Physiological responses [20–22], including stomatal regulation to minimize water loss and osmotic adjustment to maintain cellular water balance, are pivotal for stress resilience. Additionally, plants activate complex biochemical pathways to synthesize osmoprotectants, antioxidants, and stress-related proteins, crucial for mitigating oxidative damage and maintaining cellular integrity [23–25]. Emerging as a frontier in plant stress management, nanoparticles exhibit remarkable potential for enhancing stress tolerance [26–29]. These nanoparticles function as carriers for essential nutrients and antioxidants, facilitating their targeted delivery to plant tissues [30]. Furthermore, they modulate physiological processes [31], including stomatal conductance, water uptake, and photosynthetic efficiency, while also mitigating oxidative stress [32] by scavenging ROS and enhancing antioxidant enzyme activities within plant

cells. Understanding the intricate interplay between abiotic stress factors, cellular responses, and nanoparticle-mediated interventions holds immense promise for advancing strategies to enhance stress tolerance and bolster crop resilience in a changing climate.

Several types of nanoparticles have been investigated for their potential to enhance salt stress tolerance in plants. Among them, zinc oxide (ZnO) nanoparticles are one of the most commonly studied [33–35]. Other nanoparticles, such as titanium dioxide (TiO_2) [36,37], silicon dioxide (SiO_2) [38], iron oxide (Fe_2O_3) [39,40], and cerium oxide (CeO_2) [41], have also shown promise in improving salt stress tolerance in plants. Each type of nanoparticle may exert its effects through different mechanisms, including nutrient delivery, antioxidant activity, regulation of ion homeostasis, and modulation of gene expression. However, the specific choice of nanoparticle may depend on factors such as cost, availability, environmental impact, and effectiveness in different plant species and growth conditions.

Zinc oxide (ZnO) nanoparticles offer several advantages over other nanoparticles for enhancing salt stress tolerance in plants [33,42]. ZnO nanoparticles are cost-effective and readily available, making them more accessible for agricultural applications compared to some other nanoparticles. ZnO nanoparticles have been extensively studied and characterized for their biocompatibility and low toxicity to plants, ensuring minimal adverse effects on plant growth and development [43]. Moreover, ZnO nanoparticles possess inherent antioxidant properties, allowing them to efficiently scavenge reactive oxygen species, reducing oxidative damage [44]. Additionally, ZnO nanoparticles have been shown to enhance photosynthetic efficiency in salt-stressed plants, thereby contributing to improved carbon assimilation and energy production essential for plant growth and stress tolerance [45]. Zinc oxide nanoparticles hold promise as effective antifungal agents due to their ability to disrupt fungal cell membranes and walls, leading to cell leakage and eventual fungal cell death [46,47]. Therefore, the addition of ZnO nanoparticles to irrigation water reduces the number of molds in the soil, thereby increasing plant viability and the ability to withstand abiotic stress factors.

As previously mentioned, assessing the concentration of H_2O_2 in plant samples isa crucial measurement to evaluate the impact of stress on plants.

In laboratory settings, common methods for H_2O_2 determination include spectrophotometric assays utilizing enzymatic reactions or chromogenic compounds [48,49], fluorometric assays [50,51] with fluorescent probes like Amplex Red or DCFH-DA, potentiometric assays employing electrodes modified with redox mediators or enzymes, chemiluminescence assays [52] utilizing luminol-based reactions catalyzed by H_2O_2, and titrimetric assays [53] such as iodometric titration methods. Each method offers distinct advantages in sensitivity and specificity, catering to various experimental requirements and available instrumentation.

Electrochemical sensors for hydrogen peroxide detection offer several advantages over common laboratory methods [54–56]. Firstly, electrochemical sensors provide real-time, continuous monitoring capabilities, allowing for rapid detection and analysis of H_2O_2 levels with high sensitivity and precision [57,58]. Moreover, these sensors typically require smaller sample volumes and simpler sample preparation procedures, reducing the time and resources needed for analysis. Additionally, electrochemical sensors are often portable, compact, and cost-effective, making them suitable for on-site and field applications where access to laboratory facilities may be limited [59]. Furthermore, electrochemical sensors can be easily integrated into automated systems for high-throughput screening and monitoring, offering convenience and efficiency in various research and industrial settings [60]. Overall, the simplicity, speed, sensitivity, portability, and automation capabilities of electrochemical sensors make them advantageous for H_2O_2 detection compared to common laboratory methods.

Utilizing nanostructures in the fabrication of working electrodes for electrochemical sensors enables enhanced sensitivity by substantially augmenting the working surface area

without necessitating an increase in the electrode's geometric dimensions [61–63]. This approach facilitates sensor miniaturization, thereby optimizing its efficiency.

This manuscript presents an investigation into the effects of ZnO nanoparticles on enhancing salt stress tolerance in rye samples. Beyond evaluating the direct impact of these nanoparticles on plant responses to salt stress, this study delves into the potential of employing nanostructured NiO as a working electrode within an electrochemical cell. This innovative approach aims to measure the release of H_2O_2 in plant samples characterized by intricate chemical compositions. By exploring both the physiological and electrochemical aspects of nanoparticle-plant interactions, this research offers valuable insights into potential strategies for mitigating salt stress and monitoring plant health.

2. Materials and Methods

2.1. Materials

Zinc acetate dihydrate ($Zn(CH_3COO)_2{\cdot}2H_2O$, CAS No.: 5970-45-6), ethanol (C_2H_5OH, CAS No.: 64-17-5), nickel nitrate hexahydrate ($Ni(NO_3)_2{\cdot}6H_2O$, CAS No.: 13478-00-7), hexamethylenetetramine ($C_6H_{12}N_4$, CAS No.: 100-97-0), sodium hydroxide (NaOH, CAS No.: 1310-73-2), sodium chloride (NaCl, CAS No.: 7647-14-5), citric acid ($HOC(COOH)(CH_2COOH)_2$, CAS No.: 77-92-9), ascorbic acid ($C_6H_8O_6$, CAS No.: 50-81-7), glucose ($C_6H_{12}O_6$, CAS No.: 50-99-7) and hydrogen peroxide solution (H_2O_2, 30%, CAS No.: 7722-84-1) were purchased from Merck. All chemicals demonstrated a purity level equal to or greater than 99.8%. Iron wires (d = 0.5 mm, 99.9% purity) and carbon rods (d = 5 mm, 99.9% purity) were purchased from Sigma-Aldrich (St. Louis, MO, USA). Ag/AgCl wire was acquired from A-M Systems, Sequim, WA, USA. Rye seeds (*Secale cereale* L. TORAF, batch PL81604335/27TDC/1), containers for seedling cultivation, and universal peat substrate (Šepeta, Lithuania) were sourced from a local store. The distilled water required for the experiment was produced in the laboratory.

2.2. Synthesis and Analysis of ZnO Nanoparticles

To synthesize ZnO nanoparticles, 1 g of $Zn(CH_3COO)_2{\cdot}2H_2O$ was dissolved in 50 mL of ethanol, followed by the dissolution of 1 g of NaOH in 25 mL of ethanol. The resulting NaOH solution was gradually added to the main container containing the $Zn(CH_3COO)_2{\cdot}2H_2O$ solution with continuous stirring using a magnetic stirrer, resulting in a 75 mL working solution with a pH = 10. The solution was then transferred to a borosilicate glass beaker with a lid and subjected to ultrasonic treatment at 50 °C for 1 h. Subsequently, the milky colloidal solution obtained was transferred to an oven preheated to 95 °C and left for 4 h. After completion of the synthesis, the resulting white precipitate was washed multiple times with distilled water and dried in an oven for 3 h. Finally, the synthesized samples were analyzed using FESEM (MAIA 3, Tescan, Brno, Czech Republic) to evaluate nanoparticle morphology and size and an XRD diffractometer (Rigaku smart lab, RIGAKU, Tokyo, Japan) to determine the crystalline phase.

SEM illustrations of the resulting nanoparticles are depicted in Figure 1a,b. Upon drying, the nanoparticles agglomerated into spherical clusters of submicron size. A detailed examination reveals that these clusters comprise individual nanoparticles, with an average size ranging from 10 to 25 nm.

The results of the XRD analysis are depicted in Figure 1c. The graph illustrates planes corresponding to the crystalline phase of ZnO. It is evident that the resulting nanoparticles exhibit a notably high degree of crystallinity, as indicated by the minimal presence of an amorphous background. No phases characteristic of other substances were detected.

The process of the formation of ZnO nanoparticles can be described as follows [64].

In the experimental precursor solution, zinc exists in the forms of $Zn(OH)_2$ precipitates and $Zn(OH)_4^{2-}$ species, as dictated by the stoichiometric ratio of Zn^{2+} to OH^-. Under hydrothermal conditions, $Zn(OH)_2$ precipitates dissolve to a significant extent, yielding Zn^{2+} and OH^- ions. Once the product of Zn^{2+} and OH^- surpasses a critical value necessary for ZnO crystal formation, ZnO crystals precipitate from the solution. Notably, the solubility

of ZnO is much lower than that of $Zn(OH)_2$ under hydrothermal conditions, leading to a strong tendency for $Zn(OH)_2$ precipitates to transform into ZnO crystals during the hydrothermal process, as per the (1) and (2) reactions:

$$Zn(OH)_2 = Zn^{2+} + 2OH^- \quad (1)$$

$$Zn^{2+} + 2OH^- = ZnO\downarrow + H_2O \quad (2)$$

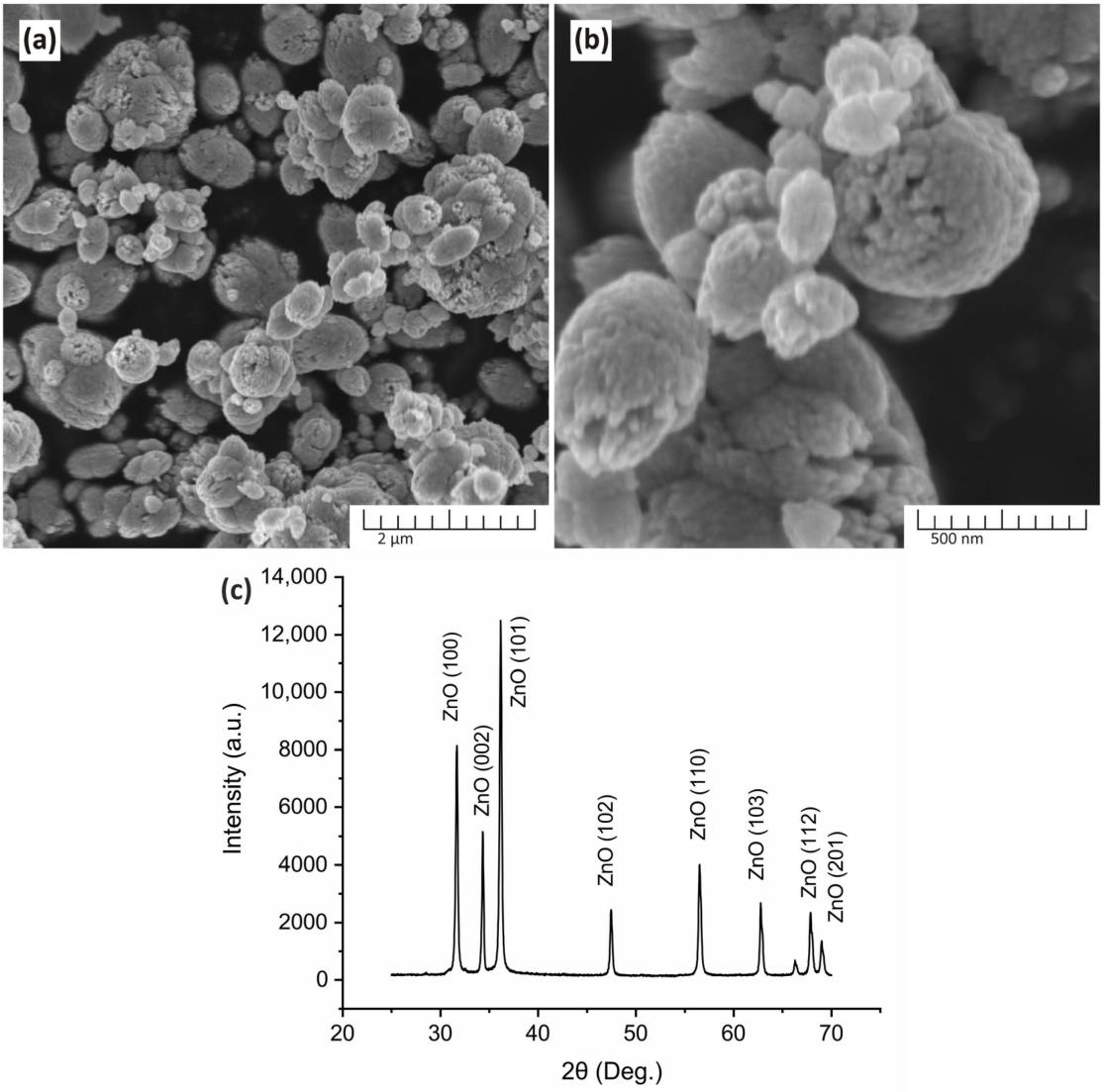

Figure 1. (**a**,**b**) SEM pictures of the ZnO nanoparticles at different magnifications. Also, here is (**c**) the XRD spectrum of the crystal structure of the ZnO nanoparticles.

Initially, elevated concentrations of Zn^{2+} and OH^- facilitate significant crystal growth in various directions. As the concentrations of Zn^{2+} and OH^- reach the supersaturation level for ZnO, nucleation and subsequent crystal growth commence.

2.3. Synthesis and Analysis of NiO Nanostructures

The iron wire was initially cut into 6 cm pieces, cleaned with sandpaper, and treated with a weak hydrochloric acid solution for 2 min to modify its microstructure and increase surface roughness, enhancing the adhesion of nanostructures. For the hydrothermal synthesis, a working solution was prepared by dissolving a 0.1 M equimolar mixture of $Ni(NO_3)2{\cdot}6H_2O$ and $C_6H_{12}N_4$ in 75 mL of distilled water with stirring. The resulting

greenish colloidal liquid was then transferred to a borosilicate glass container with a lid, with wire electrodes immersed in the solution. The setup was placed in an oven preheated to 95 °C, and hydrothermal synthesis was conducted for 5 h, yielding a light green NiOH precipitate. Following synthesis, the wires were washed several times with distilled water and annealed at 450 °C for 3 h to decompose NiOH into NiO, resulting in a dark gray matte coating on the wires. Subsequently, the electrodes were stored in a vacuum desiccator before measurements to prolong their lifespan and minimize environmental impact. The morphology of the nanostructured coating was assessed using FESEM, while the crystal structure was analyzed using an XRD diffractometer.

Figure 2a–d illustrate NiO nanostructures obtained via the hydrothermal method, showcasing the wire surface at varying magnifications. The images reveal a nanostructured coating comprising a uniform and dense layer of nanowalls, forming a porous labyrinthine structure (Figure 2a,d). Additionally, spherical flower-like formations of micrometer scale are observed atop the nanowall layer, composed of nanopetals (Figure 2b,c). The presence of these structures suggests the formation of second-generation nanostructures, where nucleation and growth occur within the working solution volume. The formed nanostructures, influenced by gravity, are deposited onto the first-generation layer, where they adhere and further develop, resulting in the formation of a network of spherical agglomerates.

Figure 2e displays an X-ray diffraction pattern of the resulting nanostructured layer. Notably, the sample exhibits a prominent amorphous background, likely attributed to the thinness of the nanostructures. Additionally, several well-defined peaks with relatively high intensity are evident, indicative of the crystalline phase of NiO. Furthermore, small inclusions of the Fe_2O_3 crystalline phase are observed in the X-ray diffraction pattern. The appearance of these inclusions can be attributed to the absence of nanostructure growth at the locations where the wire was attached in the synthesis beaker (and subsequently at the electrode attachment point in the cell), as well as the annealing process applied to the iron wire itself.

The process of hydrothermal synthesis of nanostructures can be described using Equations (3)–(5) [65]:

$$C_6H_{12}N_4 + 6H_2O \rightarrow 4NH_3 + 6HCHO \quad (3)$$

$$NH_3 + H_2O \rightarrow NH_4^+ + OH^- \quad (4)$$

$$Ni^{2+} + 2OH^- \rightarrow Ni(OH)_2 \quad (5)$$

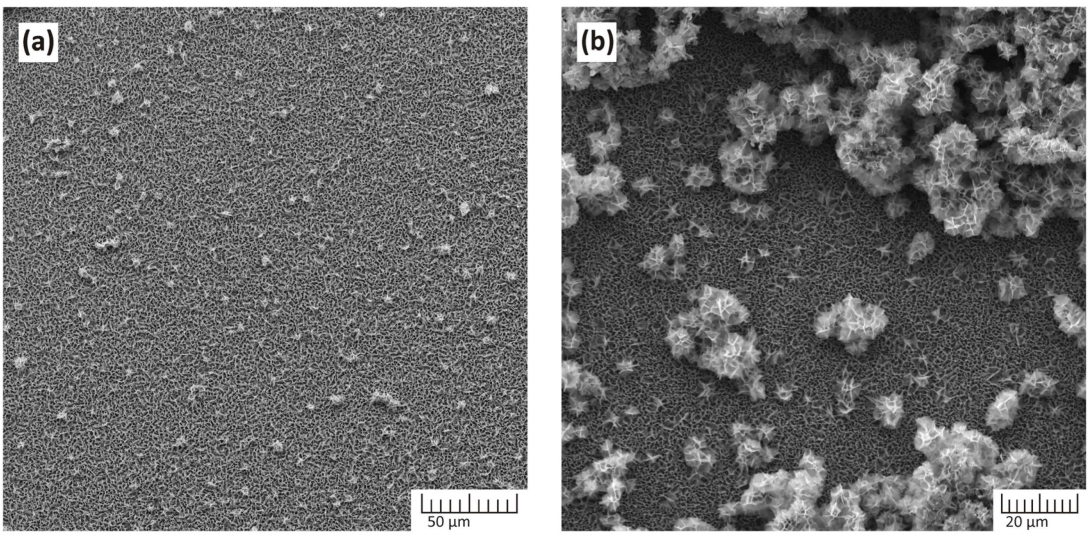

Figure 2. *Cont.*

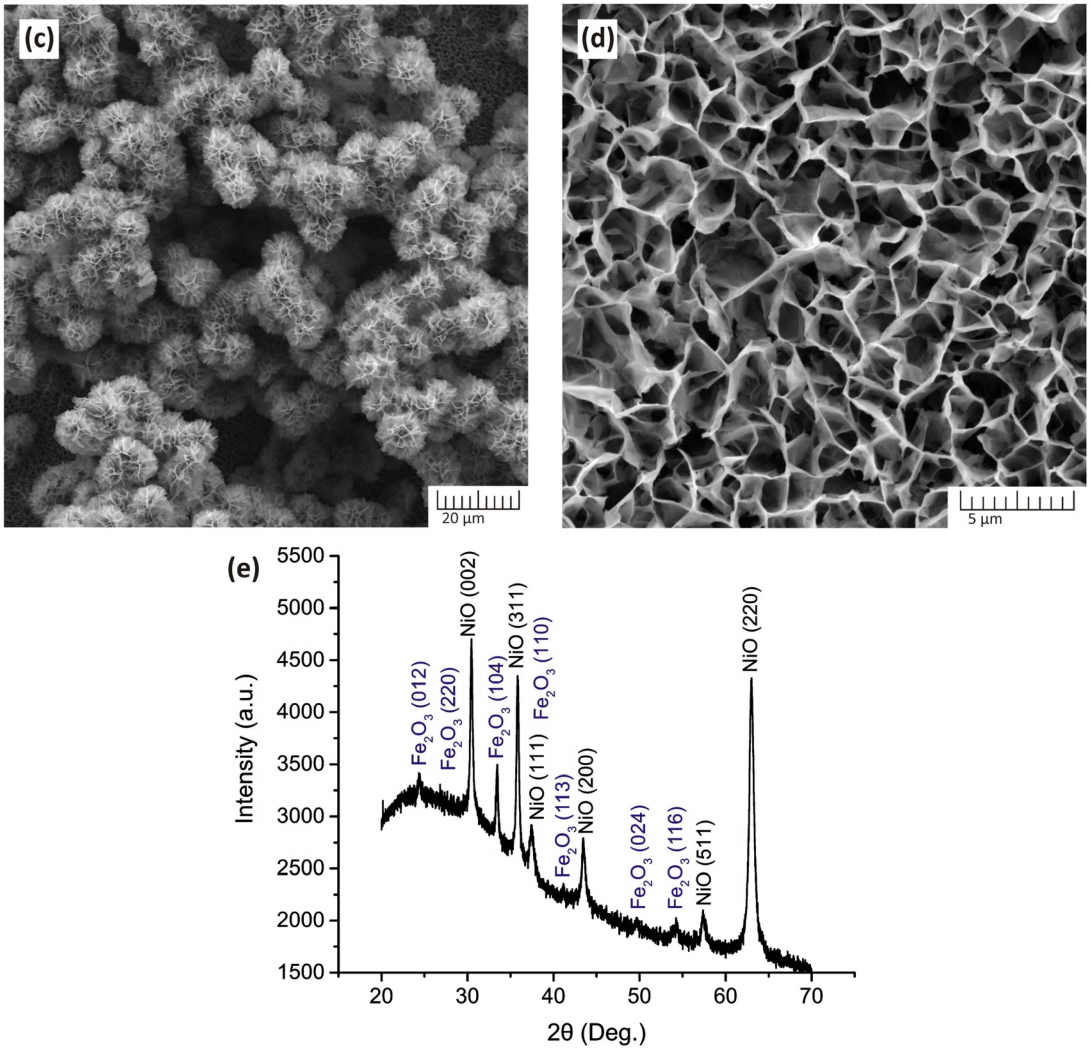

Figure 2. SEM images of the resulting nanostructured NiO coating, where (**a**–**c**) is a general view of the iron wire coated with a nanostructured wall-shaped NiO layer and (**d**) the view of NiO nanostructures at high magnification. Also, here (**e**) XRD spectrum of the resulting nanostructured NiO coating on the Fe surface.

Here, the nickel hydroxide nanostructures are obtained, and further annealing results in the formation of NiO nano-flakes due to the dehydration of nickel hydroxide as described in Equation (6):

$$Ni(OH)_2 \rightarrow NiO + H_2O \quad (6)$$

2.4. Rye Seedling Cultivation and Sample Preparation

A standard peat-containing universal substrate and six square 10 cm × 10 cm containers for each sample group were utilized for seed germination and subsequent seedling growth. Initially, during the first week of seed germination and early rye seedling development, all containers were watered daily with 20 mL of deionized water per container. From the second week onwards, the samples were divided into five groups. The first group served as the control and continued to receive 20 mL of deionized water per container daily. The second bunch of samples received daily irrigation with 20 mL of a 0.2 M aqueous NaCl solution, and the third group was watered with 20 mL of an aqueous solution containing 100 mg·L^{-1} ZnO nanoparticles. The fourth group, in order to explore the potential development of salt stress tolerance influenced by ZnO nanoparticles, was treated with a 0.2 M NaCl solution supplemented with 100 mg·L^{-1} nanoparticles. The fifth group also

received irrigation with a 0.2 M NaCl solution and a reduced concentration of nanoparticles (50 mg·L^{-1}). This treatment regimen was continued for three weeks, and the total seedling growth time was four weeks. Growth conditions, including temperature (22 °C), humidity (50%), and lighting, were maintained constant across all samples throughout the experiment. After a one-month growth period, morphological differences among the rye seedlings were assessed through manual measurements, including the determination of the length of the first leaf, total seedling length, and total green weight and dry weight per ten randomly selected seedlings from each group. Additionally, rye leaves from each experimental group were dried in a laboratory oven at 50 °C and ground into powder to conduct EDS microanalysis (INCA, OXFORD instruments, Oxford, UK), enabling the determination of trace element content in the samples. For optical and electrochemical measurements, rye leaves were cut into small pieces to facilitate extraction and then placed in a flask with a liquid extraction medium. For optical absorption measurements, 125 mg of green mass of rye seedlings per 5 mL of 96% ethanol were utilized for each sample group, while for electrochemical measurements, 10 g of rye green mass per 250 mL of 0.1 M NaOH were utilized. The above-mentioned samples were stored in a cool, dark environment overnight to aid extraction. Subsequently, the obtained extracts were twice filtered through fine filter paper to remove residual solid plant tissues.

2.5. Optical Measurements

Quantifying chlorophyll content is crucial for evaluating plant health, as its decrease indicates stress impact. In this study, chlorophyll levels in both photosystem II (PSII) and photosystem I (PSI) and the total amount of carotenoids were investigated by extracting chlorophyll from the leaves of rye seedlings subjected to untreated conditions, salt stress, and exposure to ZnO nanoparticles. To gauge the efficacy of ZnO nanoparticles in mitigating salt stress effects on rye seedlings, action spectra were measured from plants exposed to NaCl for one month. Extract samples were prepared as detailed earlier and transferred to a 5 mL transparent plastic cuvette for analysis. Each sample treatment batch underwent five replicate measurements, and the average value was taken. Analysis was performed using a UV-visible two-beam spectrophotometer SHIMADZU UV-2550PC (Shimadzu Corporation, Kyoto, Japan). Chlorophyll and carotenoid content were determined using Arnon's Equations (7)–(10) [66,67]:

$$\text{Chlorophyll } a \text{ (mg·g}^{-1}) = [12.7 \times \text{Abs}_{663} - 2.69 \times \text{Abs}_{645}] \times V_{extr}/(1000 \times M_{fr}) \quad (7)$$

$$\text{Chlorophyll } b \text{ (mg·g}^{-1}) = [22.9 \times \text{Abs}_{645} - 4.68 \times \text{Abs}_{663}] \times V_{extr}/(1000 \times M_{fr}) \quad (8)$$

$$\text{Total chlorophyll (mg·g}^{-1}) = [20.2 \times \text{Abs}_{645} + 8.02 \times \text{Abs}_{663}] \times V_{extr}/(1000 \times M_{fr}) \quad (9)$$

$$\text{Carotenoid (mg/g)} = [\text{Abs}_{480} + 0.114 \times \text{Abs}_{663} - 0.638 \times \text{Abs}_{645}] \times V_{extr}/(1000 \times M_{fr}) \quad (10)$$

where V_{extr} is extract volume in mL; M_{fr} is fresh weight in g; and Abs_{663}, Abs_{645}, and Abs_{480} are solution absorbance values at a specified wavelength.

2.6. Electrochemical Measurements

Electrochemical measurements were conducted utilizing a custom-built electrochemical cell (Figure 3a) comprising a Fe/NiO nanostructured working wire electrode, a carbon counter electrode, and an Ag/AgCl reference electrode.

The setup entails a glass beaker positioned within a water bath integrated with a magnetic stirrer for precise temperature regulation and facilitating instant mixing of the added substance throughout the entire volume of the working solution, as well as providing a more efficient diffusion process between the surface of the electrode and the volume of the analyzed liquid. A custom 3D-printed Acrylonitrile Butadiene Styrene (ABS) lid, designed for precise working electrode fixation at a specific constant height, ensures uniform electrode length and consistent sensing surface area throughout measurements, even after replacing all three electrodes for the next measurement. The electrode is securely held in a sealed plastic conic holder, allowing 1 cm of wire to be in contact with the analyte. Additionally, the lid features a substantial central opening, facilitating the introduction of

the analyte portion via micropipette during the measurement process and accommodating supplementary equipment like a thermometer or pH meter. To perform electrochemical measurements, this cell is connected to the Zahner Zennium electrochemical workstation.

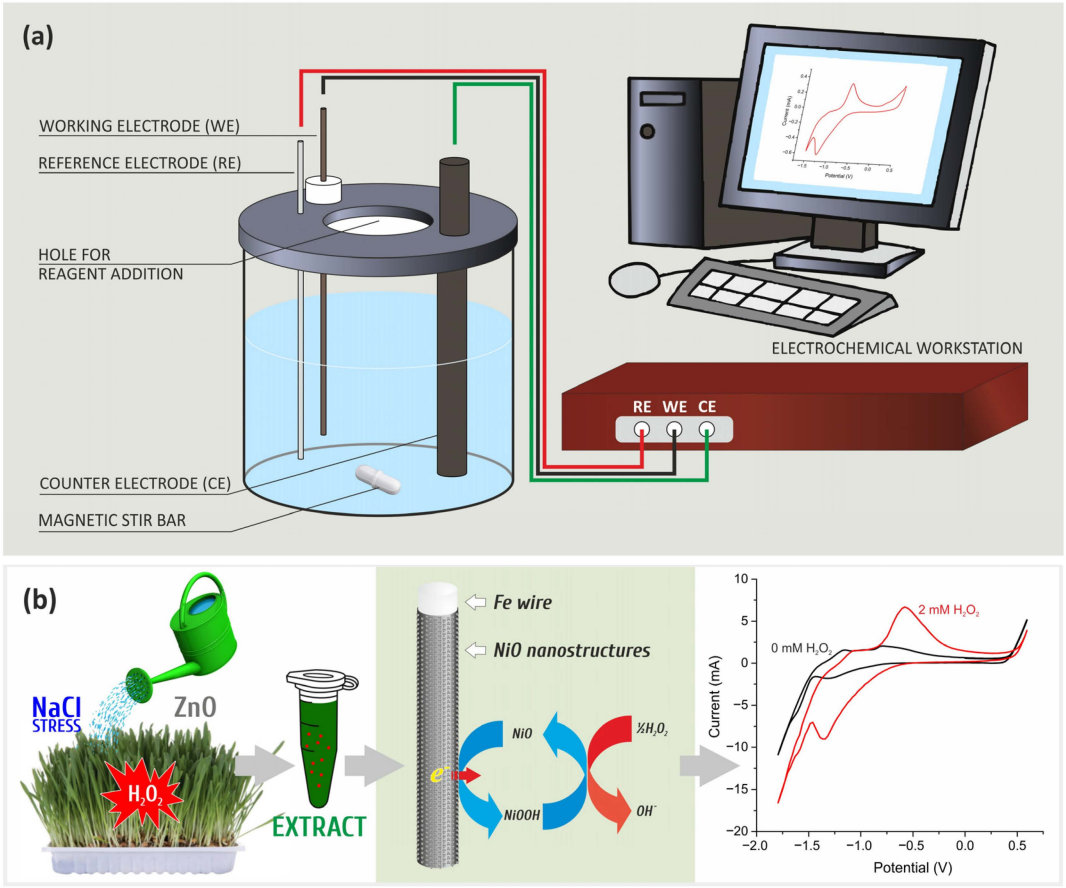

Figure 3. Graphic illustration of the experiment, where (**a**) shows the schematic representation of the electrochemical cell and (**b**) schematically displays the process of electrochemical determination of H_2O_2 in rye samples released in rye samples under the influence of salt stress.

A schematic process for the electrochemical determination of stress levels in rye samples is shown in Figure 3b.

A number of publications [48,49] indicate that before starting measurements to detect H_2O_2, an electrode with NiO nanostructures must undergo pre-treatment. To do this, it is immersed in an alkaline buffer and subjected to cyclometric scanning until the cyclograms are stabilized. In our case, we carried out cyclometry for 10 min at a speed of 100 mV·s^{-1} in the range from −1.5 V to 1.5 V.

The pre-conditioning process generates stable oxide/hydroxide species on the sensor surface, enhancing the sensitivity characteristics of the H_2O_2 sensor. This treatment is profoundly significant for sensing purposes since Ni(II)/Ni(III) species like $Ni(OH)_2$/NiOOH function as pivotal catalytic sites. Ultimately, the exceptional electrocatalytic efficiency toward H_2O_2 is linked to the generation of oxyhydroxide species (NiOOH) at relatively high applied potentials, especially in alkaline conditions. These species effectively catalyze the oxidation of H_2O_2, as indicated in Equation (11) [48,49]:

$$2NiOOH + H_2O_2 \rightarrow 2Ni(OH)_2 + O_2\uparrow \quad (11)$$

Cyclic voltammetry (CV) tests were conducted over a voltage span of −1.5 V to 0.5 V vs. Ag/AgCl, with an initial potential (Estart) set at 0 V and a scan rate of 100 mV·s^{-1}. To evaluate electrode sensitivity, diverse H_2O_2 concentrations from 100 µM to 2 mM were

added to the supporting electrolyte, and the resulting CV plots were recorded. Furthermore, the impact of scan rate and electrolyte pH on the electrochemical signal was examined.

On CV graphs, the Fe/NiO electrode exhibited two peaks at approximately −0.4 V, and −1.4 V corresponding to Ni(III)/Ni(II) reactions, as illustrated by Equations (12) and (13):

$$NiO + OH^- - e^- \leftrightarrow NiOOH \quad (12)$$

$$Ni(OH)_2 + OH^- \leftrightarrow NiOOH + H_2O + e^- \quad (13)$$

During the analysis of the current response, a constant potential of −1.4 V aligned with the peak positions on the CV graph was applied to the electrochemical cell, and the resulting current was measured. These chronoamperogram measurements were performed in a 0.1 M NaOH supporting electrolyte. Following a stabilization period of 120 s, successive additions of 25 µM H_2O_2 were introduced every 120 s to obtain a calibration curve, covering a concentration range from 25 µM to 3 mM. During all measurements, stirring was maintained using a magnetic stirrer at 1290 rpm in a water bath set at a constant temperature of 25 °C. To mitigate potential interference from complex matrices such as plant juice containing various salts, sugars, and plant tissues, interference testing involved the introduction of 100 µM portions of NaCl, glucose, citric acid, and ascorbic acid into the supporting electrolyte. Real sample analysis utilized a 0.1 M NaOH-based rye extract diluted with a 0.1M NaOH-supporting electrolyte at ratio 1:6. Since the quantity of H_2O_2 released in stressed rye samples was unknown, known concentrations of H_2O_2 were manually added to the analyte during measurements, and chronoamperograms were recorded. The concentration of identified H_2O_2 was determined based on calibration graph data for the supporting electrolyte, with the amount of H_2O_2 released in plants calculated as the difference between the total peroxide found and that artificially added during measurement. Each measurement utilized 70 mL of analyte, and the peroxide amount data utilized averaged results from multiple sample batches. To assess the stability of the electrodes, a chronoamperogram for given H_2O_2 concentrations was taken every day for a one-month-long period. Also, nanostructures after measurement were investigated with SEM.

3. Results and Discussion

Rye seedlings after a month of growth are shown in Figure 4. Morphological measurements are summarized in Table 1.

For a more correct comparison of the length of the seedling, due to the growth characteristics and the impossibility of taking measurements along with the roots, measurements were made as follows: The length of the first leaf was measured from the node from which it began to grow to the end of the leaf. The total length of the seedling should also be considered, from the first leaf node to the tip of the second.

A notable distinction is evident when comparing the overall seedling length. While samples receiving nanoparticle-containing water exhibit relatively similar average lengths, those subjected to salt stress without additional nanoparticle intervention experience considerable growth inhibition, indicating the adverse impact of elevated NaCl concentrations. Conversely, the inclusion of ZnO nanoparticles in the saline irrigation solution appears to normalize plant length, suggesting a degree of salt stress tolerance development facilitated by nanoparticles. This tolerance is further supported by the assessment of fresh weight in 10 random plants. Salt-stressed samples demonstrate a nearly halved decrease in this parameter, whereas those treated with both NaCl and ZnO nanoparticles show fresh weight tendencies similar to the control group. A comparable trend is observed in leaf dry mass comparisons. Although the control sample and those exposed solely to ZnO nanoparticles exhibit increased seedling length compared to other samples, other parameters remain largely unchanged.

Figure 4. Rye seedlings after a fourth week of growth, 10 seedlings from each batch. (**1**)—control sample, (**2**)—0.2 M NaCl treated sample, (**3**)—ZnO nPs 100 mg·L^{-1} treated sample, (**4**)—ZnO nPs 50 mg·L^{-1} and NaCl treated sample, (**5**)—ZnO nPs 100 mg·L^{-1} and NaCl treated sample. The samples were grown for one month, one week under water irrigation, and three weeks exposed to salt stress and ZnO nanoparticles.

Table 1. Morphological parameters of rye samples.

Sample	First Leaf Length (cm), Average and Maximal		Total Length of Green Part (cm), Average and Maximal		Fresh Weight of 10 Plants (g)	Dry Weight of 10 Plants (g)
Control	9	10	20	27	1.27	0.12
NaCl	8	9	14	19	0.7	0.10
nPs 100 mg·L^{-1}	10	12	21	30	1.27	0.14
nPs 50 mg·L^{-1}/NaCl	9	13	20	25	1.28	0.14
nPs 100 mg·L^{-1}/NaCl	10	13	20	27	1.27	0.14

Moreover, after a month of growth, heightened mold growth is noted in trays containing control samples and those solely receiving NaCl, whereas trays irrigated with nanoparticles display significantly weaker mold growth, indicating a favorable fungicidal effect of ZnO nanoparticles.

Table 1 reveals that there is no notable difference in the first leaf length; however, the smallest measurement value is noted in samples treated with NaCl, while the largest appears for ZnO nPs-treated samples with no difference in NaCl presented. Of particular interest is the significant increase observed in the total shoot length for samples concurrently treated with NaCl and ZnO nanoparticles. This increase in ZnO nPs-treated samples total shoot length, is approximately 2–4 cm greater than in samples treated solely with NaCl.

When considering the fresh weight of 10 plants, it becomes apparent that NaCl-treated samples exhibit the lowest values. However, this difference is considered insignificant when the control sample is compared to the samples treated only with ZnO nanoparticles. Noteworthy is the emphasis on samples watered simultaneously with NaCl and nanoparticles. Their fresh weight for ten shoots is approximately 0.6 g greater than other samples, a trend that persists even when the nanoparticle concentration is halved. Additionally, after drying, the dry weight for ten shoots is nearly identical for all samples.

The results of EDS microanalysis for the content of microelements in dried samples are summarized in Table 2.

Table 2. Microelement content for rye shoot samples (in weight percent).

Element	Control (w%)	NaCl (w%)	nPs 100 mg·L^{-1} (w%)	nPs 50 mg·L^{-1}/NaCl (w%)	nPs 100 mg·L^{-1}/NaCl (w%)
C	54.13	56.46	54.22	56.4	54.26
O	36.42	31.67	35.07	29.49	33.26
Na	0.02	1.04	0.05	0.23	0.3
Mg	0.5	0.17	0.78	0.44	0.44
P	1.39	1.02	1.95	1.85	1.95
S	0.68	0.45	0.86	0.97	0.94
Cl	0.26	4.36	0.39	4.37	2.83
K	4.9	2.64	5.21	4.88	4.65
Ca	1.52	2.04	1.26	1.18	1.19
Fe	0.06	0.04	0.09	0.08	0.06
Cu	0.12	0.11	0.12	0.11	0.12
Total	100	100	100	100	100

Essential plant nutrients include magnesium (Mg), vital for chlorophyll synthesis and enzyme activation; silicon (Si), enhancing disease resistance, cell wall strength, and stress tolerance; phosphorus (P), crucial for ATP, nucleic acids, and nutrient transport; sulfur (S), important for protein synthesis, chlorophyll formation, and photosynthesis; potassium (K), regulating osmotic balance, stomatal function, and enzyme activity; calcium (Ca), a structural component of cell walls, membranes, and signaling pathways; iron (Fe), necessary for chlorophyll synthesis and electron transport; and copper (Cu), involved in redox reactions, photosynthesis, and hormone metabolism. From Table 2, we see that in the samples watered exclusively with NaCl solution, there is a significant excess of Na ions in comparison with the control sample. Adding ZnO nanoparticles to the irrigation solution leads to a decrease in the amount of Na ions. The addition of nanoparticles to the solution for irrigation has practically no effect on the number of Cl ions; it remains the same for a concentration of ZnO NPS of 50 mg·L^{-1} and only slightly decreases with an increase to 100 mg·L^{-1} concentration. It is also clear that in samples watered only with NaCl, the amount of important nutrients, such as P, Mg, S, etc., is decreased in comparison with the control sample. It can be seen that the addition of nanoparticles helps to increase the level of these nutrients. If we compare samples that were treated with ZnO nanoparticles and were not exposed to salt stress with controls, we see an increase in the content of some important nutrients. In general, these facts indicate that the addition of ZnO nanoparticles to the irrigation solution containing NaCl helps to significantly reduce the harmful effects of salt stress on rye samples and improves their vital functions.

The action spectrum for rye samples is illustrated in Figure 5, with corresponding numerical data summarized in Table 3. Notably, distinct peaks are observed at 430 nm and 663 nm, characteristic of chlorophyll *a*, and at 450 nm and 645 nm, indicative of chlorophyll *b*, while carotenoids exhibit a peak at 480 nm. Comparing with the control, a significant reduction in total chlorophyll content (over 50%) is evident in salt-stressed samples without ZnO nanoparticle supplementation. Conversely, samples supplemented with nanoparticles, not exposed to salt stress, exhibit a 26% increase in total chlorophyll concentration compared to controls. Moreover, the addition of ZnO nanoparticles to NaCl-containing water elevates the chlorophyll concentration to control levels. The peaks at 429 nm and 455 nm merit special consideration. In samples subjected to salt stress (both with and without nanoparticle supplementation), the peak at 429 nm, indicative of chlorophyll *a*, predominates in height. Conversely, in samples unaffected by salt stress, the peak at 455 nm, representing chlorophyll *b*, is more prominent. Carotenoid content

mirrors total chlorophyll content, being minimal in salt-stressed samples and maximal in nanoparticle-treated samples. Overall, the findings suggest that ZnO nanoparticle supplementation enhances photosynthesis in rye samples, bolstering their vitality and augmenting their tolerance to salt stress.

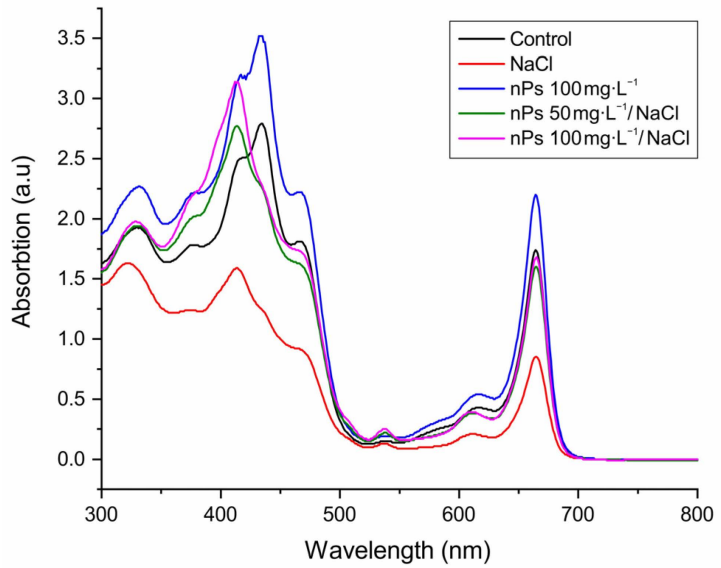

Figure 5. Chlorophyll absorbance measurements for rye samples grown for four weeks under treatment with NaCl and ZnO nanoparticles.

Table 3. Changes in chlorophyll and carotenoid concentrations in rye samples grown under the influence of salt stress and ZnO nanoparticles.

	Chl (*a*), mg·g^{-1}	Chl (*b*), mg·g^{-1}	Chl (total), mg·g^{-1}	Carot., mg·g^{-1}
Control	0.8049	0.2643	1.0689	0.0443
NaCl	0.3923	0.1359	0.5280	0.0233
nPs 100 mg·L^{-1}	1.0152	0.3357	1.3506	0.0540
nPs 50 mg·L^{-1}/NaCl	0.7446	0.1979	0.9424	0.0430
nPs 100 mg·L^{-1}/NaCl	0.7715	0.2590	1.0303	0.0441

This phenomenon could be attributed to ZnO ability to capture surplus sodium ions, thus lowering their levels in the root area and thwarting their excessive absorption by plants. Furthermore, nanoparticles might aid in the conveyance of vital nutrients and minor elements, potentially amplifying their assimilation by plants and offsetting the diminished nutrient intake resulting from salt stress.

In Figure 6, crucial electrochemical assessments are illustrated aimed at elucidating the sensor's characteristics and optimal operational parameters. In the presence of 0.1 M NaOH, the NiO electrode displays two well-defined peaks at −1.4 V and −0.4 V. These redox peaks signify a reversible transition between $Ni(OH)_2/NiOOH$, as indicated by Equations (12) and (13). Additionally, Figure 6a demonstrates that the introduction of H_2O_2 concentrations in the range of 100 µM to 2 mM into the supporting electrolyte elicits a notable electrochemical response and increase in peak current value, indicating catalytic processes on the NiO electrode influenced by hydrogen peroxide.

In Figure 6b, the relationship between the electrochemical response and scanning speed is depicted for a constant concentration of H_2O_2 (2 µM) in the supporting electrolyte. It's evident that with increasing scanning speed, both peaks substantially heighten. However, upon surpassing the 100 mV·s^{-1} threshold, the peak becomes less distinct at a

potential of −1.4 V, accompanied by additional noise in the cyclic voltammogram. Taking these observations into account, a scanning speed of 100 mV·s^{-1} was deemed optimal for subsequent experiments.

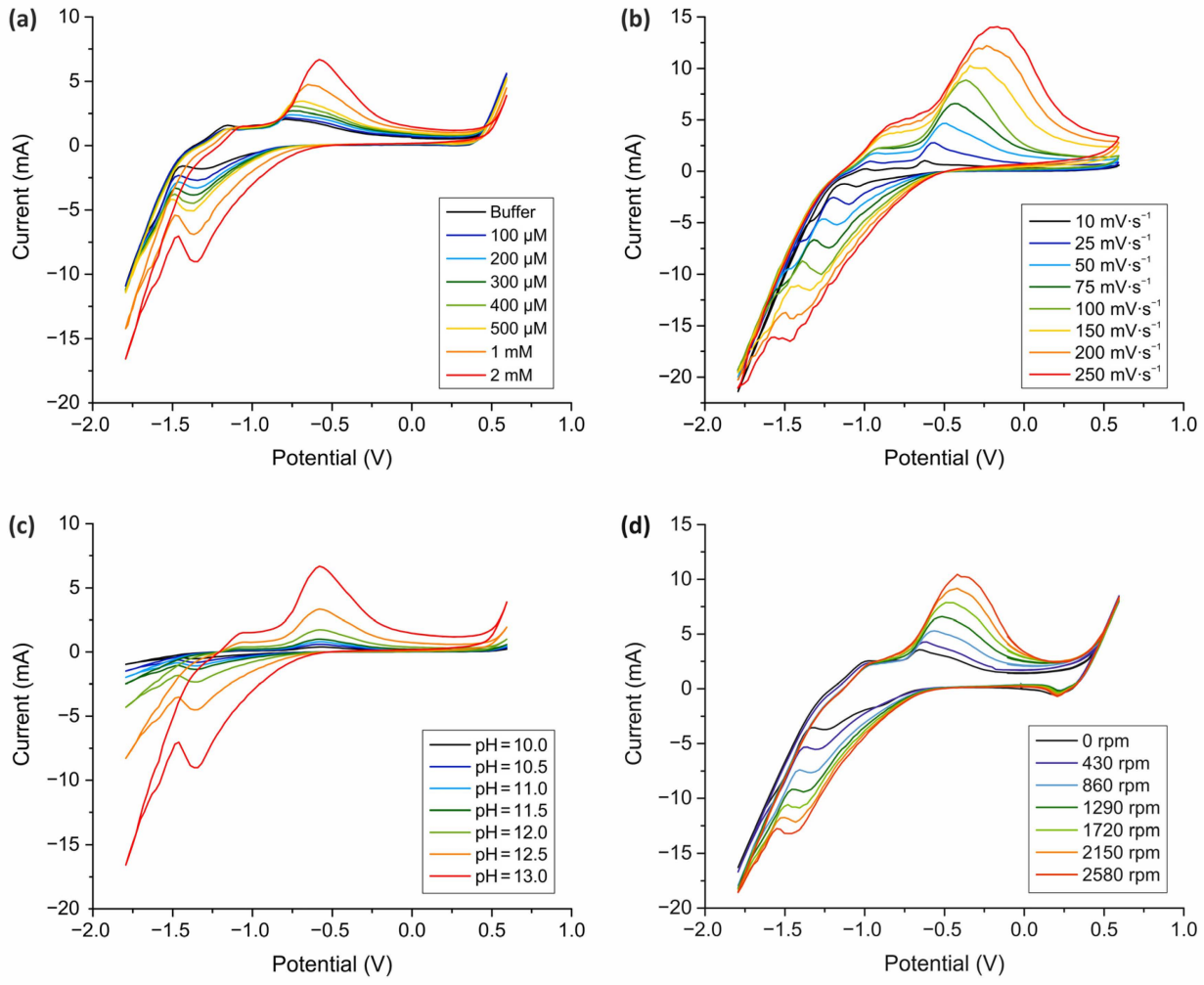

Figure 6. (**a**) CV graph of a nanostructured NiO nanowall-based electrode obtained in a 0.1 M NaOH supporting electrolyte and in solutions containing H_2O_2 in a concentration range of 100 µM to 2 mM. (**b**) Dependence of the electrochemical response of the NiO electrode on the scanning speed. Scanning was performed in a 0.1 M NaOH solution containing 2 mM H_2O_2. (**c**) Dependence of the electrochemical response of the NiO electrode on solution pH. Measurements were performed in a supporting electrolyte containing 2 mM H_2O_2 and different concentrations of NaOH at a scanning rate of 100 mV·s^{-1}. (**d**) Dependence of the electrochemical response of the NiO electrode on the stirring speed of the analyzed solution. The measurements were carried out in a 0.1 M NaOH solution containing 2 mM H_2O_2 with a scanning speed of 100 mV·s^{-1}. The stirring speed was controlled with a magnetic stirrer.

As the scanning speed increases, we observe a horizontal shift of both peaks towards higher potential values. The shift in potential value for the peak in cyclic voltammetry with increasing scanning speed can be attributed to the kinetics of the electrochemical reactions occurring at the electrode surface. As the scanning speed increases, the rate of mass transport of species to and from the electrode surface also increases. This can lead to changes in the concentration gradients of electroactive species near the electrode, affecting the kinetics of the redox reactions. Consequently, the peak potential may shift due to changes in the reaction rates and the associated overpotential required for the reactions

to proceed. Additionally, higher scanning speeds can result in increased double-layer charging currents, which may influence the observed peak potential.

In Figure 6c, the dependence of the electrochemical response on the pH of the supporting electrolyte is illustrated at a constant H_2O_2 concentration of 2 mM and a scanning speed of 100 mV·s^{-1}. It's evident that for pH values ranging from 10 to 11.5, characteristic peaks are practically absent in the cyclogram. However, upon reaching pH 12, a clear electrochemical response emerges with two well-defined peaks, whose height continues to increase with further pH elevation. However, pursuing higher pH levels becomes impractical as it necessitates working with high-concentration alkalis, leading to increased reagent usage, potential environmental hazards, and the corrosion of cell elements. Hence, the optimal solution is represented by 0.1 M NaOH, offering a pH of 13 without the need for excessive reagents, ensuring both efficiency and environmental friendliness.

The catalytic reaction and electrochemical response of a NiO electrode typically increase with higher pH levels due to several factors. Firstly, the surface of the NiO electrode becomes more negatively charged in alkaline conditions, facilitating the adsorption of positively charged species involved in the catalytic process. This increased surface charge density promotes their interaction with the electrode surface, enhancing the overall electrochemical process. Additionally, alkaline environments generally offer more favorable reaction kinetics, allowing for faster electron transfer and more efficient conversion of reactants to products. The higher concentration of hydroxide ions in alkaline solutions further promotes the availability of reactive species, leading to enhanced catalytic activity and electrochemical response. Moreover, certain active species formed during the catalytic reaction may exhibit greater stability in alkaline conditions, contributing to prolonged catalytic activity and sustained electrochemical response over time. Overall, the influence of pH on the NiO electrode promotes favorable conditions for catalytic reactions, resulting in improved electrochemical performance. In Figure 6d, the electrochemical response of the nanostructured electrode is plotted against the stirring speed of the analyzed solution. Notably, an increase in stirring speed corresponds to a rise in the height of the redox peaks. This trend mirrors the observations seen in the dependency of electrochemical response on scanning speed (Figure 6b), attributed to heightened mass transfer rates of particles from the solution bulk to the electrode surface, altering reaction kinetics. The optimal stirring speed was determined to be 1290 rpm, striking a balance between significant response enhancement and the prevention of excessive bubble formation that could interfere with signal reception. Moreover, excessively high stirring speeds risk inducing funnel formation and mechanical damage to electrodes, particularly the delicate carbon electrode.

In Figure 7a, the stability of the NiO nanostructured electrode over time is demonstrated, under the condition that the samples were stored at room temperature without protection from environmental factors.

To monitor this, the peak current value was measured for a potential of −1.4 V in a 0.1 M NaCl supporting electrolyte with a 2 M H_2O_2 concentration and a scanning speed of 100 mV·s^{-1}. Measurements were taken every second day. It is evident that over a span of 30 days, the peak current value decreased by no more than 4%, indicating the electrode's high stability and minimal degradation over time. Figure 7b depicts the variation in the current peak value with repeated usage of the same electrode multiple times. Measurements were conducted under identical electrochemical parameters, with the electrode being rinsed with distilled water and annealed at 450 degrees for 30 min after each measurement. It can be observed that the electrode's efficiency remains nearly unchanged up to the sixth measurement, with a subsequent 7% decrease in value on the tenth attempt. Figure 7c presents a SEM image of the electrode surface after ten uses, revealing that while the surface retains characteristic plates, the thinnest ones have fused together, resulting in a slight reduction in surface area and, consequently, a decline in efficiency.

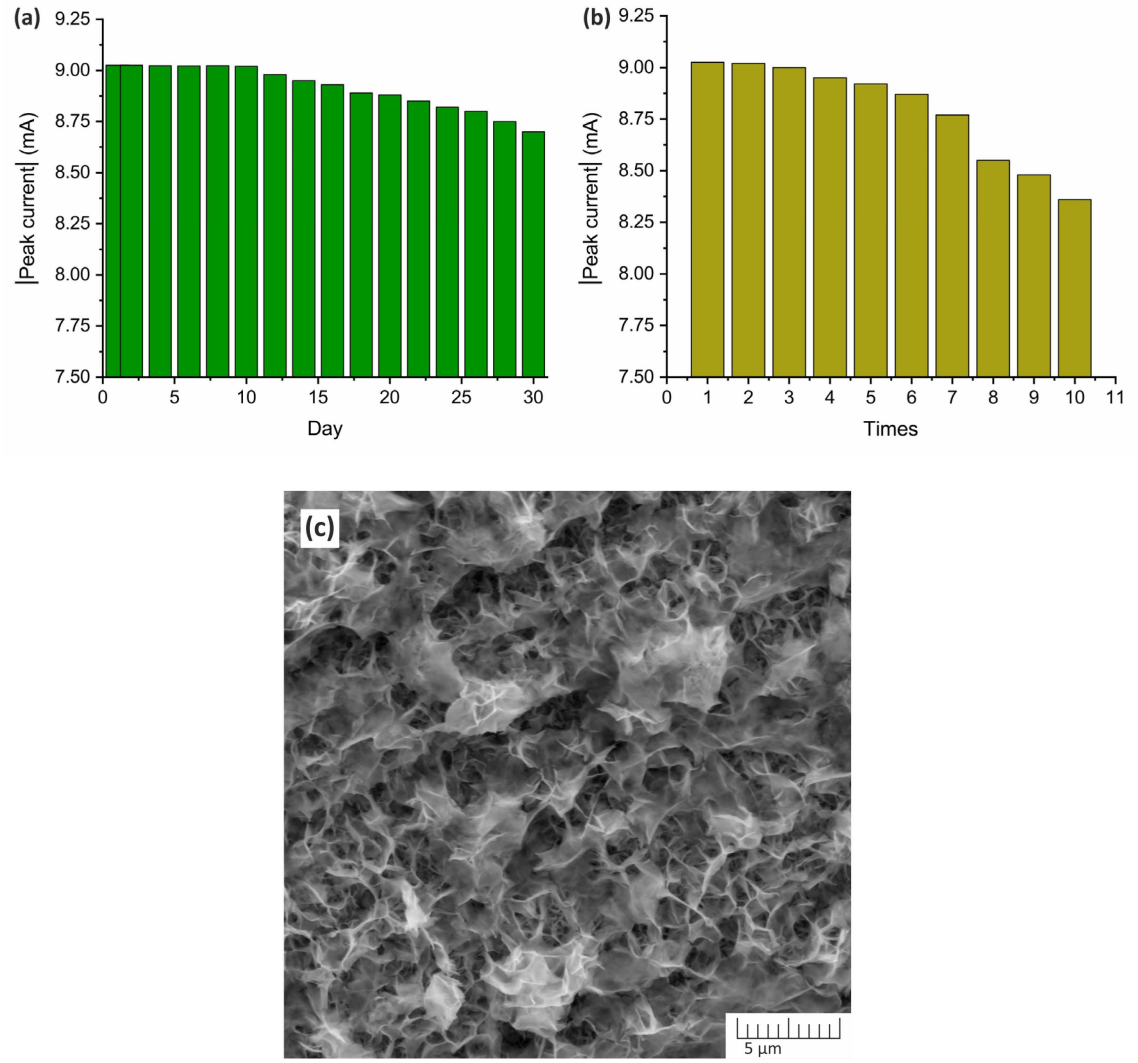

Figure 7. The long-term stability assessment of the wall-like nanostructured NiO electrode is depicted in (**a**). It evaluates the variation in the maximum current peak value over time. Graph (**b**) illustrates the electrode's potential for repeated use, demonstrating the alteration in the maximum peak current concerning the electrode's reuse frequency. Additionally, (**c**) presents a SEM image portraying the electrode surface after multiple uses.

Figure 8a showcases the chronoamperogram obtained upon the addition of H_2O_2 to the supporting electrolyte, ranging from 25 µM to 4 mM. It's evident that both low doses (25 µM) and substantial doses (500 µM) of H_2O_2 induce a clear and distinct electrochemical response, forming a characteristic step whose height correlates with the added H_2O_2 amount. A calibration curve (Figure 8b) was obtained based on this data, displaying a linear relationship across the entire concentration range of H_2O_2. The sensitivity of the NiO nanostructured sensor stands at 2474 $\mu A \cdot mM^{-1}$, with a calculated limit of detection (LOD) of 1.59 µM, assuming a signal-to-noise ratio of 3. As previously noted, plant juice presents a complex composition comprising various elements such as sugars, organic acids, and solid cellular structures.. Hence, in the development of an electrochemical sensor tailored for these analytes, it's imperative to mitigate the risk of erroneous electrochemical responses due to interfering substances. To address this concern, interference testing was conducted by introducing substances like NaCl, glucose, citric acid, and ascorbic acid alongside H_2O_2. As depicted in Figure 8d, none of the interferents elicited a significant electrochemical response, underscoring the sensor's high sensitivity in discerning H_2O_2 in intricate plant analytes.

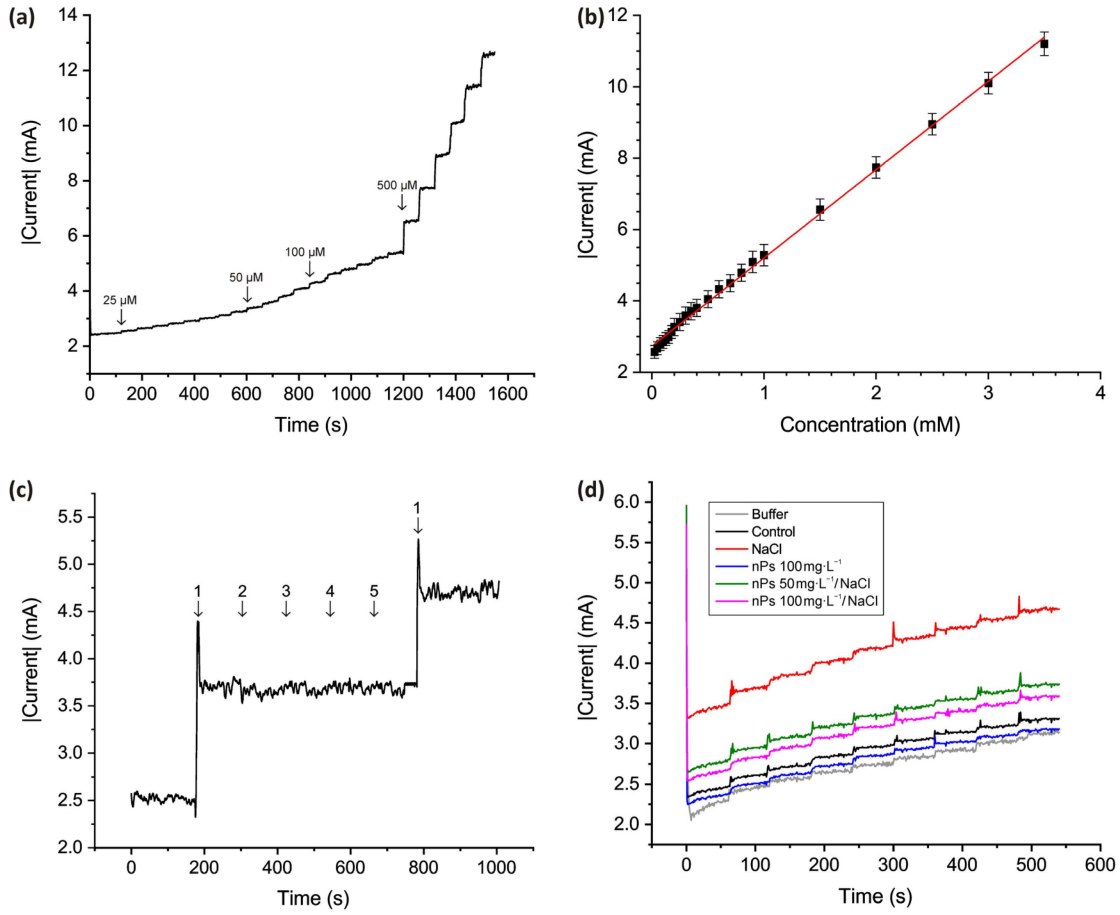

Figure 8. (**a**) The chronoamperogram captured in a 0.1 M NaOH supporting electrolyte for the NiO nanostructured electrode at a peak potential of −1.4 V, achieved by introducing H_2O_2 in concentrations ranging from 25 µM to 4 mM. (**b**) A calibration curve illustrating the concentration–current relationship. (**c**) An interference study examining the impact of H_2O_2 addition **(1)** alongside common plant interferents, including NaCl (**2**), glucose (**3**), citric acid (**4**), and ascorbic acid (**5**). (**d**) Analysis of real samples presenting chronoamperograms obtained through incremental addition of H_2O_2, ranging from 25 µM to 200 µM with 25 µM increments, to the rye seedling extract samples.

Figure 8d presents chronoamperograms from the analysis of real rye samples for H_2O_2 content. The numerical values of detected H_2O_2 released in samples under the influence of salt stress are summarized in Table 4. The highest levels of H_2O_2 released during the growth process were detected in samples irrigated with NaCl and reached the 500 µM level. However, introducing ZnO nanoparticles to the saline irrigation solution notably reduced the H_2O_2 concentration, with the extent of reduction dependent on the ZnO nanoparticle concentration (more than 60% for 50 mg·L^{-1} and more than 75% for 100 mg·L^{-1} compared to samples irrigated with only NaCl).

In the chronoamperogram, at lower added concentrations (steps 1–3), the measured H_2O_2 content tends to be lower than the actual amount but stabilizes around the fourth step (from 100µM concentrations) across all graphs, aligning with the slopes of both the buffer chronoamperogram and the plant extract chronoamperograms. This initial underestimation of the electrochemical response appears to be linked to specific plant components present in the rye samples, influencing the measurement process. Notably, this phenomenon is absent in pure buffer solutions, where the chronoamperogram displays a corresponding slope even with the first H_2O_2 infusions. While additional filtration helps improve the electrochemical response, it doesn't completely resolve the issue, prompting further exploration into alternative extraction methods or mathematical adjustments. Nevertheless, it's important to reiterate that despite these minor challenges, the detected H_2O_2 concentrations

significantly surpass those of control samples, indicating the onset of oxidative stress under NaCl influence and the sensor's effectiveness in detecting H_2O_2 in plant samples with complex chemical compositions.

Table 4. Analysis of real rye extract samples for the presence of H_2O_2 as a marker of oxidative stress.

Buffer			**Control**			**NaCl**		
Added (μM)	Found (μM)	Excess (μM)	Added (μM)	Found (μM)	Excess (μM)	Added (μM)	Found (μM)	Excess (μM)
25	25	0	25	53	28	25	389	364
50	50	0	50	80	30	50	465	415
75	75	0	75	105	30	75	526	451
100	100	0	100	148	48	100	608	508
125	125	0	125	172	47	125	638	513
150	150	0	150	199	49	150	673	523
175	175	0	175	226	51	175	703	528
200	200	0	200	255	55	200	727	527
nPs 100 mg·L^{-1}			**nPs 50 mg·L^{-1}/NaCl**			**nPs 100 mg·L^{-1}/NaCl**		
Added (μM)	Found (μM)	Excess (μM)	Added (μM)	Found (μM)	Excess (μM)	Added (μM)	Found (μM)	Excess (μM)
25	30	5	25	128	103	25	86	61
50	57	7	50	158	108	50	114	64
75	101	26	75	220	145	75	148	73
100	126	26	100	263	163	100	198	98
125	149	24	125	295	170	125	225	100
150	172	22	150	327	177	150	273	123
175	193	18	175	358	183	175	294	119
200	208	8	200	382	182	200	318	118

Table 5 offers a comparative analysis of the sensor developed in this study with other Ni-based sensors reported in the literature. It is evident that in many instances, our sensor exhibits sensitivity and a LOD on par with or even superior to those reported in previous studies. The deliberate choice of a small surface area was made to minimize wire electrode vibrations during solution stirring, yet the resulting sensitivity remains adequate for the intended analyte. However, if required, sensitivity can be enhanced by increasing the working surface area through the substitution of wire electrodes with metal plates. Notably, our sensor provides stable performance in plant analytes, eliminating the need for complex sample pre-processing. Looking ahead, this electrode holds potential for integration into a compact multisensory system comprising wire electrodes coated with nanostructures of various metal oxides (such as CuO, Co_3O_4,TiO_2, ZnO, etc.).

Table 5. Comparative analysis of electrochemical sensors based on NiO presented in other sources.

Electrode	Sensitivity	Linear Range	LOD	Reference
NiO NPs/GCE	-	8.6 nM–433.24 μM	4.28 nM	[46]
GCE/CNT-PEI@NiO	830 mA·M^{-1}·cm $^{-2}$	0.004–0.8 mM	1.0 μM	[47]
NiO TF-ITO	807 mA·M^{-1}·cm^{-2}	0.011–2.4 mM	3.22 μM	[48]
NiO-NSs/CF-1801/GCE	23.30 μA·mM^{-1}·cm^{-2}	0.20–3.75 mM	13.03 nM	[49]

Table 5. *Cont.*

Electrode	Sensitivity	Linear Range	LOD	Reference
Co3O4/NiO-NSs/CF-1801	7.67 $mA \cdot mM^{-1} \cdot cm^{-2}$	0.20–4.00 mM	5.51 µM	[50]
$Ni(OH)_2$ nPs	1660 $\mu A \cdot mM^{-1} \cdot cm^{-2}$	30–320 µM	26.4 µM	[51]
Fe-NiO NW	15.46 $mA \cdot mM^{-1} \cdot cm^{-2}$	0.025–4.00 mM	1.59 µM	This work

4. Conclusions

This study successfully developed a working electrode for an electrochemical sensor based on Fe wire and wall-shaped NiO nanostructures, demonstrating high sensitivity (2474 $\mu A \cdot mM^{-1}$ or 15.46 $mA \cdot mM^{-1} \cdot cm^{-2}$) and a low limit of detection (1.59 µM) with good selectivity against common interferents found in plant samples. Moreover, the sensor exhibited excellent long-term stability, retaining over 95% of its effectiveness after 30 days. Employing this sensor, the research investigated the negative impact of salt stress on rye seedlings and assessed the potential mitigating effects of ZnO nanoparticles. Results revealed significant H_2O_2 release in plants under salt stress conditions (up to 500 µM), indicating oxidative stress. However, the addition of ZnO nanoparticles to the irrigation water containing NaCl led to a reduction in released H_2O_2 by 60–70%, suggesting enhanced salt stress tolerance. This reduction in oxidative stress, detected by the NiO-based electrochemical sensor, was further supported by chlorophyll optical absorption measurements. It was found that samples treated with NaCl exhibited a 50% decrease in total chlorophyll content compared to controls, while those treated with NaCl and ZnO nanoparticles showed chlorophyll levels comparable to the control. Additionally, the application of ZnO nanoparticles without salt stress increased total chlorophyll content by over 25% compared to controls. These comprehensive results highlight the potential of the developed nanowalled NiO electrochemical sensor to work with real plant analytes and suggest promising applications of NiO nanoparticles to alleviate oxidative stress in plants subject to salt stress.

Author Contributions: Conceptualization, V.G. and M.K.; methodology, M.K.; formal analysis, V.M. and J.K.; investigation, M.K. and E.S.; visualization, E.S.; writing—original draft preparation M.K.; writing—review and editing, E.S., I.M. and A.B.; supervision, V.G. All authors have read and agreed to the published version of the manuscript.

Funding: This research received no external funding.

Data Availability Statement: Data are contained within the article.

Conflicts of Interest: The authors declare no conflicts of interest.

References

1. Hura, T.; Hura, K.; Ostrowska, A. Drought-Stress Induced Physiological and Molecular Changes in Plants. *Int. J. Mol. Sci.* **2022**, *23*, 4698. [CrossRef]
2. Guo, P.-R.; Wu, L.-L.; Wang, Y.; Liu, D.; Li, J.-A. Effects of Drought Stress on the Morphological Structure and Flower Organ Physiological Characteristics of *Camellia oleifera* Flower Buds. *Plants* **2023**, *12*, 2585. [CrossRef]
3. Ondrasek, G.; Rathod, S.; Manohara, K.K.; Gireesh, C.; Anantha, M.S.; Sakhare, A.S.; Parmar, B.; Yadav, B.K.; Bandumula, N.; Raihan, F.; et al. Salt Stress in Plants and Mitigation Approaches. *Plants* **2022**, *11*, 717. [CrossRef]
4. Chaudhry, U.K.; Gökçe, Z.N.Ö.; Gökçe, A.F. The Influence of Salinity Stress on Plants and Their Molecular Mechanisms. *Biol. Life Sci. Forum* **2022**, *11*, 31. [CrossRef]
5. Sanwong, P.; Sanitchon, J.; Dongsansuk, A.; Jothityangkoon, D. High Temperature Alters Phenology, Seed Development and Yield in Three Rice Varieties. *Plants* **2023**, *12*, 666. [CrossRef]
6. Vasilachi, I.C.; Stoleru, V.; Gavrilescu, M. Analysis of Heavy Metal Impacts on Cereal Crop Growth and Development in Contaminated Soils. *Agriculture* **2023**, *13*, 1983. [CrossRef]
7. Xie, X.; He, Z.; Chen, N.; Tang, Z.; Wang, Q.; Cai, Y. The Roles of Environmental Factors in Regulation of Oxidative Stress in Plant. *BioMed Res. Int.* **2019**, *2019*. [CrossRef]
8. Chaki, M.; Begara-Morales, J.C.; Barroso, J.B. Oxidative Stress in Plants. *Antioxidants* **2020**, *9*, 481. [CrossRef]

9. Zulfiqar, F.; Ashraf, M. Proline Alleviates Abiotic Stress Induced Oxidative Stress in Plants. *J. Plant Growth Regul.* **2023**, *42*, 4629–4651. [CrossRef]
10. Černý, M.; Habánová, H.; Berka, M.; Luklová, M.; Brzobohatý, B. Hydrogen Peroxide: Its Role in Plant Biology and Crosstalk with Signalling Networks. *Int. J. Mol. Sci.* **2018**, *19*, 2812. [CrossRef]
11. Chatgilialoglu, C. Biomarkers of Oxidative and Radical Stress. *Biomolecules* **2024**, *14*, 194. [CrossRef]
12. Rahman, M.; Asaeda, T.; Fukahori, K.; Imamura, F.; Nohara, A.; Matsubayashi, M. Hydrogen Peroxide Measurement Can Be Used to Monitor Plant Oxidative Stress Rapidly Using Modified Ferrous Oxidation Xylenol Orange and Titanium Sulfate Assay Correlation. *Int. J. Plant Biol.* **2023**, *14*, 546–557. [CrossRef]
13. Ferrigo, D.; Scarpino, V.; Vanara, F.; Causin, R.; Raiola, A.; Blandino, M. Influence of H_2O_2-Induced Oxidative Stress on In Vitro Growth and Moniliformin and Fumonisins Accumulation by *Fusarium proliferatum* and *Fusarium subglutinans*. *Toxins* **2021**, *13*, 653. [CrossRef]
14. Kumar, H.; Dhalaria, R.; Guleria, S.; Cimler, R.; Sharma, R.; Siddiqui, S.A.; Valko, M.; Nepovimova, E.; Dhanjal, D.S.; Singh, R.; et al. Anti-oxidant potential of plants and probiotic spp. in alleviating oxidative stress induced by H_2O_2. *Biomed. Pharmacother.* **2023**, *165*, 115022. [CrossRef]
15. Acosta-Motos, J.R.; Ortuño, M.F.; Bernal-Vicente, A.; Diaz-Vivancos, P.; Sanchez-Blanco, M.J.; Hernandez, J.A. Plant Responses to Salt Stress: Adaptive Mechanisms. *Agronomy* **2017**, *7*, 18. [CrossRef]
16. Qamer, Z.; Chaudhary, M.T.; Du, X.; Hinze, L.; Azhar, M.T. Review of oxidative stress and antioxidative defense mechanisms in *Gossypium hirsutum* L. in response to extreme abiotic conditions. *J. Cotton Res.* **2021**, *4*, 9. [CrossRef]
17. González, E.M. Drought Stress Tolerance in Plants. *Int. J. Mol. Sci.* **2023**, *24*, 6562. [CrossRef]
18. Alkahtani, J.; Dwiningsih, Y. Analysis of Morphological, Physiological, and Biochemical Traits of Salt Stress Tolerance in Asian Rice Cultivars at Seedling and Early Vegetative Stages. *Stresses* **2023**, *3*, 717–735. [CrossRef]
19. Hussein, M.A.A.; Alqahtani, M.M.; Alwutayd, K.M.; Aloufi, A.S.; Osama, O.; Azab, E.S.; Abdelsattar, M.; Hassanin, A.A.; Okasha, S.A. Exploring Salinity Tolerance Mechanisms in Diverse Wheat Genotypes Using Physiological, Anatomical, Agronomic and Gene Expression Analyses. *Plants* **2023**, *12*, 3330. [CrossRef]
20. Hasanuzzaman, M.; Fujita, M. Plant Responses and Tolerance to Salt Stress: Physiological and Molecular Interventions. *Int. J. Mol. Sci.* **2022**, *23*, 4810. [CrossRef]
21. Li, Z.; Cheng, B.; Zhao, Y.; Luo, L.; Zhang, Y.; Feng, G.; Han, L.; Peng, Y.; Zhang, X. Metabolic Regulation and Lipidomic Remodeling in Relation to Spermidine-induced Stress Tolerance to High Temperature in Plants. *Int. J. Mol. Sci.* **2022**, *23*, 12247. [CrossRef]
22. Li, Q.; Qin, Y.; Hu, X.; Jin, L.; Li, G.; Gong, Z.; Xiong, X.; Wang, W. Physiology and Gene Expression Analysis of Potato (*Solanum tuberosum* L.) in Salt Stress. *Plants* **2022**, *11*, 1565. [CrossRef]
23. El-Badri, A.M.; Batool, M.; AA Mohamed, I.; Wang, Z.; Khatab, A.; Sherif, A.; Ahmad, H.; Khan, M.N.; Hassan, H.M.; Elrewainy, I.M.; et al. Antioxidative and Metabolic Contribution to Salinity Stress Responses in Two Rapeseed Cultivars during the Early Seedling Stage. *Antioxidants* **2021**, *10*, 1227. [CrossRef]
24. Wang, X.; Mi, S.; Miao, H. Transcriptomic Responses to Chilling Reveal Potential Chilling Tolerance Mechanisms in Cucumber. *Int. J. Mol. Sci.* **2022**, *23*, 12834. [CrossRef]
25. Brenes, M.; Solana, A.; Boscaiu, M.; Fita, A.; Vicente, O.; Calatayud, Á.; Prohens, J.; Plazas, M. Physiological and Biochemical Responses to Salt Stress in Cultivated Eggplant (*Solanum melongena* L.) and in *S. insanum* L., a Close Wild Relative. *Agronomy* **2020**, *10*, 651. [CrossRef]
26. Sári, D.; Ferroudj, A.; Abdalla, N.; El-Ramady, H.; Dobránszki, J.; Prokisch, J. Nano-Management Approaches for Salt Tolerance in Plants under Field and In Vitro Conditions. *Agronomy* **2023**, *13*, 2695. [CrossRef]
27. Khalid, M.F.; Iqbal Khan, R.; Jawaid, M.Z.; Shafqat, W.; Hussain, S.; Ahmed, T.; Rizwan, M.; Ercisli, S.; Pop, O.L.; Alina Marc, R. Nanoparticles: The Plant Saviour under Abiotic Stresses. *Nanomaterials* **2022**, *12*, 3915. [CrossRef]
28. Abideen, Z.; Hanif, M.; Munir, N.; Nielsen, B.L. Impact of Nanomaterials on the Regulation of Gene Expression and Metabolomics of Plants under Salt Stress. *Plants* **2022**, *11*, 691. [CrossRef]
29. Rajput, V.D.; Minkina, T.; Kumari, A.; Harish; Singh, V.K.; Verma, K.K.; Mandzhieva, S.; Sushkova, S.; Srivastava, S.; Keswani, C. Coping with the Challenges of Abiotic Stress in Plants: New Dimensions in the Field Application of Nanoparticles. *Plants* **2021**, *10*, 1221. [CrossRef]
30. Wahid, I.; Kumari, S.; Ahmad, R.; Hussain, S.J.; Alamri, S.; Siddiqui, M.H.; Khan, M.I.R. Silver Nanoparticle Regulates Salt Tolerance in Wheat Through Changes in ABA Concentration, Ion Homeostasis, and Defense Systems. *Biomolecules* **2020**, *10*, 1506. [CrossRef]
31. Li, P.; Xia, Y.; Song, K.; Liu, D. The Impact of Nanomaterials on Photosynthesis and Antioxidant Mechanisms in Gramineae Plants: Research Progress and Future Prospects. *Plants* **2024**, *13*, 984. [CrossRef]
32. Lee, J.H.J.; Kasote, D.M. Nano-Priming for Inducing Salinity Tolerance, Disease Resistance, Yield Attributes, and Alleviating Heavy Metal Toxicity in Plants. *Plants* **2024**, *13*, 446. [CrossRef]
33. Singh, A.; Sengar, R.S.; Rajput, V.D.; Minkina, T.; Singh, R.K. Zinc Oxide Nanoparticles Improve Salt Tolerance in Rice Seedlings by Improving Physiological and Biochemical Indices. *Agriculture* **2022**, *12*, 1014. [CrossRef]
34. Seleiman, M.F.; Ahmad, A.; Alshahrani, T.S. Integrative Effects of Zinc Nanoparticle and PGRs to Mitigate Salt Stress in Maize. *Agronomy* **2023**, *13*, 1655. [CrossRef]

35. Rakgotho, T.; Ndou, N.; Mulaudzi, T.; Iwuoha, E.; Mayedwa, N.; Ajayi, R.F. Green-Synthesized Zinc Oxide Nanoparticles Mitigate Salt Stress in *Sorghum bicolor*. *Agriculture* **2022**, *12*, 597. [CrossRef]
36. Badshah, I.; Mustafa, N.; Khan, R.; Mashwani, Z.-u.-R.; Raja, N.I.; Almutairi, M.H.; Aleya, L.; Sayed, A.A.; Zaman, S.; Sawati, L.; et al. Biogenic Titanium Dioxide Nanoparticles Ameliorate the Effect of Salinity Stress in Wheat Crop. *Agronomy* **2023**, *13*, 352. [CrossRef]
37. Mustafa, N.; Raja, N.I.; Ilyas, N.; Abasi, F.; Ahmad, M.S.; Ehsan, M.; Mehak, A.; Badshah, I.; Proćków, J. Exogenous Application of Green Titanium Dioxide Nanoparticles (TiO_2 NPs) to Improve the Germination, Physiochemical, and Yield Parameters of Wheat Plants under Salinity Stress. *Molecules* **2022**, *27*, 4884. [CrossRef]
38. Avestan, S.; Ghasemnezhad, M.; Esfahani, M.; Byrt, C.S. Application of Nano-Silicon Dioxide Improves Salt Stress Tolerance in Strawberry Plants. *Agronomy* **2019**, *9*, 246. [CrossRef]
39. Feng, Y.; Kreslavski, V.D.; Shmarev, A.N.; Ivanov, A.A.; Zharmukhamedov, S.K.; Kosobryukhov, A.; Yu, M.; Allakhverdiev, S.I.; Shabala, S. Effects of Iron Oxide Nanoparticles (Fe_3O_4) on Growth, Photosynthesis, Antioxidant Activity and Distribution of Mineral Elements in Wheat (*Triticum aestivum*) Plants. *Plants* **2022**, *11*, 1894. [CrossRef]
40. Gerbreders, V.; Krasovska, M.; Sledevskis, E.; Mihailova, I.; Mizers, V. Co_3O_4 Nanostructured Sensor for Electrochemical Detection of H_2O_2 as a Stress Biomarker in Barley: Fe_3O_4 Nanoparticles-Mediated Enhancement of Salt Stress Tolerance. *Micromachines* **2024**, *15*, 311. [CrossRef]
41. Hassanpouraghdam, M.B.; Vojodi Mehrabani, L.; Bonabian, Z.; Aazami, M.A.; Rasouli, F.; Feldo, M.; Strzemski, M.; Dresler, S. Foliar Application of Cerium Oxide-Salicylic Acid Nanoparticles (CeO_2:SA Nanoparticles) Influences the Growth and Physiological Responses of *Portulaca oleracea* L. under Salinity. *Int. J. Mol. Sci.* **2022**, *23*, 5093. [CrossRef]
42. Alabdallah, N.M.; Alzahrani, H.S. The potential mitigation effect of ZnO nanoparticles on [*Abelmoschus esculentus* L. Moench] metabolism under salt stress conditions. *Saudi. J. Biol. Sci.* **2020**, *27*, 3132–3137. [CrossRef]
43. Plaksenkova, I.; Kokina, I.; Petrova, A.; Jermaļonoka, M.; Gerbreders, V.; Krasovska, M. The Impact of Zinc Oxide Nanoparticles on Cytotoxicity, Genotoxicity, and miRNA Expression in Barley (*Hordeum vulgare* L.) Seedlings. *Sci. World J.* **2020**, *2020*, 6649746. [CrossRef]
44. Lalarukh, I.; Zahra, N.; Al Huqail, A.A.; Amjad, S.F.; Al-Dhumri, S.A.; Ghoneim, A.M.; Alshahri, A.H.; Almutari, M.M.; Alhusayni, F.S.; Al-Shammari, W.B.; et al. Environmental Technology & Innovation Exogenously applied ZnO nanoparticles induced salt tolerance in potentially high yielding modern wheat (*Triticum aestivum* L.) cultivars. *Environ. Technol. Innov.* **2022**, *27*, 102799. [CrossRef]
45. Karimian, Z.; Samiei, L. ZnO nanoparticles efficiently enhance drought tolerance in *Dracocephalum kotschyi* through altering physiological, biochemical and elemental contents. *Front. Plant Sci.* **2023**, *14*, 1063618. [CrossRef]
46. Praveen Kumar, G.; Maheshwaran, S.; Chen, S.-M.; Akilarasan, M.; Chen, T.-W.; Tseng, T.-W.; Yu, J.; Yu, R. A Facile synthesis of the Nickel Oxide Nanoparticles for the Effective Electrochemical Detection of Hydrogen peroxide in Contact Lens Solution. *Int. J. Electrochem. Sci.* **2020**, *15*, 8181–8189. [CrossRef]
47. Fernández, I.; Carinelli, S.; González-Mora, J.L.; Villalonga, R.; Salazar-Carballo, P.A. Nickel oxide nanoparticles/carbon nanotubes nanocomposite for non-enzymatic determination of hydrogen peroxide. *Electroanalysis* **2022**, *35*, 2200192. [CrossRef]
48. Salazar, P.; Rico, V.; González-Elipe, A.R. Non-enzymatic hydrogen peroxide detection at NiO nanoporous thin film-electrodes prepared by physical vapor deposition at oblique angles. *Electrochim. Acta* **2017**, *235*, 534–542. [CrossRef]
49. Liu, M.; An, M.; Xu, J.; Liu, T.; Wang, L.; Liu, Y.; Zhang, J. Three-dimensional carbon foam supported NiO nanosheets as non-enzymatic electrochemical H_2O_2 sensors. *Appl. Surf. Sci.* **2021**, *542*, 148699. [CrossRef]
50. An, M.; Liu, M.; Liu, Y. Three-Dimensional Carbon Foam Supported Co_3O_4/NiO Nanosheets As Non-Enzymatic Electrochemical H_2O_2 Sensors. *ECS Meet. Abstr.* **2021**, *MA2021-01*, 1166. [CrossRef]
51. Medhi, A.; Giri, M.K.; Mohanta, D. Non-enzymatic electrochemical detection of H_2O_2 using $Ni(OH)_2$ nanoparticles. *Mater. Today Proc.* **2022**, *68*, 262–267. [CrossRef]
52. Teniou, A.; Madi, I.A.; Mouhoub, R.; Marty, J.L.; Rhouati, A. One-Step Chemiluminescent Assay for Hydrogen Peroxide Analysis in Water. *Chemosensors* **2023**, *11*, 455. [CrossRef]
53. Gimeno, M.P.; Mayoral, M.C.; Andrés, J.M. A potentiometric titration for H_2O_2 determination in the presence of organic compounds. *Anal. Methods* **2013**, *5*, 1510. [CrossRef]
54. Hussein, M.A.; Khan, A.; Alamry, K.A. A highly efficient electrochemical sensor containing polyaniline/cerium oxide nanocomposites for hydrogen peroxide detection. *RSC Adv.* **2022**, *12*, 31506–31517. [CrossRef]
55. Sobahi, N.; Imran, M.; Khan, M.E.; Mohammad, A.; Alam, M.M.; Yoon, T.; Mehedi, I.M.; Hussain, M.A.; Abdulaal, M.J.; Jiman, A.A. Electrochemical Sensing of H_2O_2 by Employing a Flexible Fe_3O_4/Graphene/Carbon Cloth as Working Electrode. *Materials* **2023**, *16*, 2770. [CrossRef]
56. Sohrabi, H.; Maleki, F.; Khaaki, P.; Kadhom, M.; Kudaibergenov, N.; Khataee, A. Electrochemical-Based Sensing Platforms for Detection of Glucose and H_2O_2 by Porous Metal–Organic Frameworks: A Review of Status and Prospects. *Biosensors* **2023**, *13*, 347. [CrossRef]
57. Kader, M.A.; Azmi, N.S.; Kafi, A.K.M.; Hossain, M.S.; Jose, R.; Goh, K.W. Ultrasensitive Nonenzymatic Real-Time Hydrogen Peroxide Monitoring Using Gold Nanoparticle-Decorated Titanium Dioxide Nanotube Electrodes. *Biosensors* **2023**, *13*, 671. [CrossRef]

58. Sun, Y.; He, K.; Zhang, Z.; Zhou, A.; Duan, H. Real-time electrochemical detection of hydrogen peroxide secretion in live cells by Pt nanoparticles decorated graphene–carbon nanotube hybrid paper electrode. *Biosens. Bioelectron.* **2015**, *68*, 358–364. [CrossRef]
59. Zamfir, L.-G.; Jinga, M.L.; Tulea, R.; Vărzaru, G.; Constantin, M.; Răut, I.; Firincă, C.; Jecu, M.-L.; Doni, M.; Gurban, A.-M. Portable Electrochemical System for the Monitoring of Biogenic Amines in Soil as Indicators in Assessment of the Stress in Plant. *Chem. Proc.* **2023**, *13*, 2. [CrossRef]
60. Li, G.; Chen, Y.; Liu, F.; Bi, W.; Wang, C.; Lu, D.; Wen, D. Portable visual and electrochemical detection of hydrogen peroxide release from living cells based on dual-functional Pt-Ni hydrogels. *Microsyst. Nanoeng.* **2023**, *9*, 152. [CrossRef]
61. Mihailova, I.; Krasovska, M.; Sledevskis, E.; Gerbreders, V.; Mizers, V.; Ogurcovs, A. Assessment of Oxidative Stress by Detection of H_2O_2 in Rye Samples Using a CuO- and Co_3O_4-Nanostructure-Based Electrochemical Sensor. *Chemosensors* **2023**, *11*, 532. [CrossRef]
62. Trujillo, R.M.; Barraza, D.E.; Zamora, M.L.; Cattani-Scholz, A.; Madrid, R.E. Nanostructures in Hydrogen Peroxide Sensing. *Sensors* **2021**, *21*, 2204. [CrossRef]
63. Shringi, A.K.; Kumar, R.; Dennis, N.F.; Yan, F. Two-Dimensional Tellurium Nanosheets for the Efficient Nonenzymatic Electrochemical Detection of H_2O_2. *Chemosensors* **2024**, *12*, 17. [CrossRef]
64. Aneesh, P.M.; Vanaja, K.A.; Jayaraj, M.K. Synthesis of ZnO nanoparticles by hydrothermal method. In Proceedings of the Nanophotonic Materials IV, San Diego, CA, USA, 17 September 2007; Volume 6639. [CrossRef]
65. Abbasi, M.A.; Ibupoto, Z.H.; Hussain, M.; Pozina, G.; Lu, J.; Hultman, L.; Nur, O.; Willander, M. Decoration of ZnO Nanorods with Coral Reefs like NiO Nanostructures by the Hydrothermal Growth Method and Their Luminescence Study. *Materials* **2014**, *7*, 430–440. [CrossRef]
66. Olatunbosun, A.; Nigar, H.; Rovshan, K.; Nurlan, A.; Boyukhanim, J.; Narmina, A.; Ibrahim, A. Comparative impact of nanoparticles on salt resistance of wheat plants. *MethodsX* **2023**, *11*, 102371. [CrossRef]
67. Arnon, D.I. Copper enzymes in isolated chloroplasts. Polyphenoloxidase in Beta vulgaris. *Plant Physiol.* **1949**, *24*, 1–15. [CrossRef]